

# Devolatilization of Subducting Slabs, Part II: Volatile Fluxes and Storage

Meng Tian,\* Richard F. Katz, and Dave A. May

*Department of Earth Sciences, University of Oxford, South Parks Road, Oxford, OX1 3AN, UK.*

David W. Rees Jones

*Department of Earth Sciences, University of Oxford, South Parks Road, Oxford, OX1 3AN, UK.*

*Department of Earth Sciences, Bullard Laboratories,*

*University of Cambridge, Madingley Road, Cambridge, CB3 0EZ, UK.*

(Dated: September 3, 2022)

Subduction is a crucial part of the long-term  $H_2O$  and  $CO_2$  cycling between Earth's exosphere and interior. However, there is broad disagreement over how much  $H_2O$  and  $CO_2$  is liberated from subducting slabs to mantle wedge and transported to island-arc volcanoes. In the companion paper Part I, we parameterize the metamorphic reactions involving  $H_2O$  and  $CO_2$  for representative subducting lithologies. On this basis, a two-dimensional reactive transport model is constructed in this Part II. We assess the various controlling factors of  $CO_2$  and  $H_2O$  release from subducting slabs. Model results show that up-slab fluid flow directions produce flux peak of  $CO_2$  and  $H_2O$  at subarc depths. Moreover, infiltration of  $H_2O$ -rich fluids sourced from hydrated slab mantle enhances decarbonation or carbonation at lithological interfaces, increases slab surface fluxes, and redistributes  $CO_2$  from basalt and gabbro layers to the overlying sedimentary layer. As a result, diapiric removal of slab surface sediments leads to elevated  $CO_2$  and  $H_2O$  fluxes along the slab surface; the migration of sedimentary diapirs can serve as a crucial avenue for carbon transfer from slabs to mantle wedge. The modelled subduction efficiency of  $H_2O$  ranges from  $\sim 20\%$  to  $\sim 90\%$ , and that of  $CO_2$  from  $\sim 80\%$  to  $\sim 100\%$ , indicating a large fraction of  $CO_2$  is recycled to mantle depth beyond  $\sim 200$  km. This higher estimate of subduction efficiency arises from consideration of open-system fractionation effects within the interior of the lithological layers. It is potentially an overestimate because local flow focusing and ionic carbon species are neglected in our model.

## I. INTRODUCTION

Earth distinguishes itself from other solar system planets through its habitability that is maintained by its surface climate. Over geological time, water and  $CO_2$  modulate the climate through geochemical cycles between Earth's exosphere and interior [1]. Subduction is a major tectonic process that brings altered, near-surface rock into the deep Earth and therefore participates in the long-term geochemical cycles. However, the flux of carbon generated by subduction is still actively debated. Dasgupta and Hirschmann [2] and Hirschmann [3] argue that subducting slabs don't experience significant degassing or melting and so sequester their carbon into deep Earth over geological history. On the other hand, Kelemen and Manning [4] contends that most carbon is liberated from slabs and migrates into the subduction-zone mantle lithosphere, rather than going into the deep mantle.

Detailed field and modelling studies also give disparate views on the fate of subducting carbon. Kerrick and Connolly [5, 6, 7] constructed petrological pseudosections for representative lithologies in subduction zones (i.e., hydrothermally altered slab mantle, metabasalts, metasediments). They concluded that all representative lithologies bring a significant amount of  $CO_2$  into the deep mantle, except that clay-rich slab sediments undergo complete decarbonation at forearc depths along hot subduction geotherms. Subsequently, Gorman *et al.* [8] evaluated the open-system effects induced by aqueous fluid infiltration on the thermodynamic modelling of subduction-zone dehydration and decarbonation. They concluded that  $CO_2$  liberation is still limited, in spite of  $H_2O$ -rich fluid infiltration. Field studies on subducted carbonates, however, suggest considerable carbon release by carbonate dissolution [9]. Further thermodynamic models considering aqueous ionic species also suggest that carbon release from subducting slabs is significant because dissolution of carbon in the form of organic ions can enhance carbon removal from rocks [10]. In particular, Connolly and Galvez [11] argue that  $H_2O$ -rich fluid infiltration together with ionic form dissolution can completely decarbonate subducting sediments.

Purely thermodynamic models of the fate of subducted carbon are zero-dimensional in that the system is assumed to be closed, with no directional mass transfer. In contrast, the one-dimensional open-system model by Gorman *et al.*

---

\* meng.tian@earth.ox.ac.uk

[8] treated  $\text{H}_2\text{O}$  &  $\text{CO}_2$  allowed for vertical fluid migration. Two-dimensional geodynamic models of porous fluid migration indicates substantial fluid migration nearly parallel to subducting slabs [12]. This focused flow is caused by the formation of a high-permeability channel in the dewatering layer and a compaction pressure gradient that helps contain liquids in the slab. Given that flow directions within the slab are uncertain and reactive flow is path-dependent, it is important to assess the effect of fluid flow direction on the fluxes of  $\text{H}_2\text{O}$  &  $\text{CO}_2$  out of subducting slabs.

An extra challenge exists in the computational treatment of open-system behaviors when incorporating metamorphic reactions involving volatiles into fluid flow modelling. Since fluid movement constantly changes the bulk composition of each subdomain within the modelled slab, the computational cost will be prohibitively high if a traditional pseudo-section calculation is applied to each subdomain repeatedly throughout the model evolution. In the companion paper Part I, we have parameterized the coupled dehydration and decarbonation processes for representative subducting lithologies (i.e., sediments, MORB, gabbro, and peridotite). This light-weight thermodynamic module focuses on the behaviors of  $\text{H}_2\text{O}$  &  $\text{CO}_2$  and can readily capture the fractionation and infiltration effects typical in open systems. Thus it forms the basis of the efficient reactive flow model in the current study.

In this paper, we provide a simple two dimensional model of reactive fluid flow in subducting slabs. Since the dynamics of within-slab flow remains highly uncertain [e.g., 12–15], we prescribe the flow direction in our model and investigate model behaviour as a function of this parameter, rather than solving equations for momentum conservation. The model incorporates open-system equilibrium thermodynamics and enables us to assess the factors controlling slab dehydration and decarbonation. In particular, we find that nearly up-slab fluid flow produces a peak in the volatile flux at subarc depths and might thus be relevant for arc magmatism. We find that a sedimentary layer can act as a cap that absorbs  $\text{CO}_2$  released from underlying slab lithologies, if the sediments are not removed in diapirs. Furthermore, slab lithospheric mantle, if extensively serpentized, can cause significant  $\text{H}_2\text{O}$  &  $\text{CO}_2$  fluxes at subarc depths in warm subduction settings. In all the cases we explored, 20–90 wt%  $\text{H}_2\text{O}$  and 80–100 wt%  $\text{CO}_2$  in the slabs subduct beyond mantle depth of  $\sim 200$  km.

In the following, we start with a description of our model setup in section II, followed by the numerics of model solution in section III. Model results are then provided regarding closed-system behavior in section IV A, which is provided for comparison of our model with previous work assuming constant bulk compositions. On top of this, we present results on a reference, open-system model in section IV B, both for comparison with the closed-system model and to serve as a reference case to investigate parameter sensitivity. The subsequent models presented explore the variability of  $\text{H}_2\text{O}$  and  $\text{CO}_2$  fluxes on slab surface in response to changes in fluid flow direction (section IV C), slab age (section IV D), extent of slab mantle serpentization (section IV E), and diapiric removal of slab surface sediments (section IV F). For all the open-system models we run, the efficiency of  $\text{H}_2\text{O}$  and  $\text{CO}_2$  subduction into the deep mantle is summarized in section IV G, which is followed by a discussion (section V) of the model limitations.

## II. MODEL SETUP

The geometry of the model is illustrated in Figure 1; we focus only on the subducting slab. Cold temperatures in the slab create strong resistance to viscous (de-)compaction [12] and hence the slab experiences negligible isotropic deformation over the model times in this study ( $\sim 6$  Ma). We therefore treat the slab as a rigid plate in our model. Slab deformation has also been modelled using visco-elastic [15] and visco-elasto-plastic rheologies [13], yielding diverse fluid flow patterns within slab. By treating the slab as a rigid plate, the flow direction in our model becomes a free parameter that is to be explored (see below), and we can thus circumvent the uncertainties in fluid flow directions arising from slab rheologies that are difficult to constrain.

Under the rigid plate assumption, the solid velocities ( $\mathbf{v}_s$ ) in the slab are uniformly of magnitude equal to the subduction rate and can be prescribed as a model parameter. If a slab age and dip are further chosen, the steady-state temperature ( $T$ ) and pressure ( $P$ ) of the slab can be calculated using canonical thermo-mechanical models [e.g., 16]. Our model assumes such a steady-state  $P$ – $T$  structure of the slab and extracts it from the geodynamic model by England and Katz [17]. Figure 2 illustrates an example of this for a 10-Ma-old slab with a convergence rate of 5 cm  $\text{yr}^{-1}$  and a dip of 45°; this  $P$ – $T$  field is employed in some of our models in section IV.

Superimposed on this rigid and thermally steady-state slab is the reactive  $\text{H}_2\text{O}$  &  $\text{CO}_2$  transport model. This transport model assumes local equilibrium between the solid and percolating liquid phases. The solid phase in the slab is lithologically layered as shown in Fig. 1b, and consist of sediments, mid-ocean ridge basalts (MORB), gabbros, and peridotites from top to bottom. In the companion paper Part I, we parameterize the equilibrium partitioning of  $\text{H}_2\text{O}$  &  $\text{CO}_2$  between the liquid and solid for each of the four representative lithologies, and this parameterization serves as a thermodynamic module coupled to the fluid flow model detailed below.

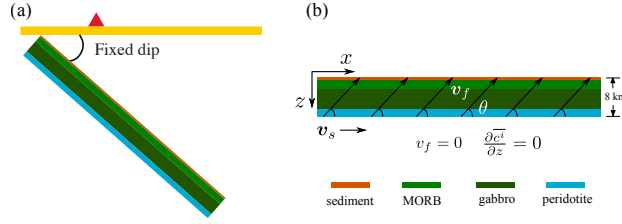


FIG. 1. Sketch showing the model geometry and boundary conditions. (a) The geodynamic setting of our model. It shows that the model assumes a fixed slab dipping angle and the slab acts like a rigid plate that doesn't deform. A red triangle denotes the position of arc volcano. (b) The modelled slab domain. The  $x$ - and  $z$ - axes are respectively parallel and normal to the slab extension; this coordinate system is used in all the succeeding figures displaying the entire slab. The slab lithologically consists of four representative rock types as detailed in the legend. Solid velocities within the slab are uniformly set to slab convergence rate ( $v_s$ ).  $\theta$  is the angle between  $x$ -axis and the uniform fluid flow direction. Notations of symbols are listed in Table I and details on the initial and boundary conditions are provided in section III.

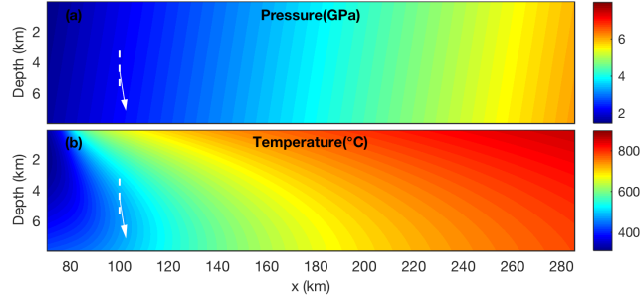


FIG. 2. A representative illustration of the  $P$  &  $T$  structure for a 10-Ma-old slab. A convergence rate of  $5 \text{ cm yr}^{-1}$  and a slab dip of  $45^\circ$  are used. The  $x$ -axis starts from  $\sim 70 \text{ km}$  because we assume the overriding plate (Fig. 1) has a 50-km-thick lithosphere which corresponds to  $\sim 70 \text{ km}$  for the starting position of the slab immediately below it. Note that the vertical and horizontal scales are different due to the high aspect ratio of the modelled slab. White dashed lines are a reference direction perpendicular to slab extension and solid white arrows denote the direction of gravity in the stretched domain; the same line and arrow conventions apply in the succeeding figures.

Following previous studies [18–21], mass conservation for liquid and solid phases in porous media are expressed as:

$$\frac{\partial \phi}{\partial t} + \nabla \cdot (\mathbf{v}_f \phi) = \frac{\Gamma}{\rho_f}, \quad (1)$$

$$\frac{\partial(1 - \phi)}{\partial t} + \nabla \cdot [\mathbf{v}_s(1 - \phi)] = -\frac{\Gamma}{\rho_s}, \quad (2)$$

where densities of both phases are assumed to be constant, and notations for symbols are listed in Table I. In addition, the conservation of volatile species  $\text{H}_2\text{O}$  &  $\text{CO}_2$  in both phases are:

$$\frac{\partial(\rho_f \phi c_f^i)}{\partial t} + \nabla \cdot (\rho_f \mathbf{v}_f \phi c_f^i) = \Gamma_i, \quad (3)$$

$$\frac{\partial[\rho_s(1 - \phi)c_s^i]}{\partial t} + \nabla \cdot [\rho_s \mathbf{v}_s(1 - \phi)c_s^i] = -\Gamma_i, \quad (4)$$

where  $i$  represents either  $\text{H}_2\text{O}$  or  $\text{CO}_2$ . Chemical diffusion is neglected here because the Péclet number ( $v_f H/D$ ) is  $\sim 250$  if slab thickness  $H$  of 8 km, diffusion coefficient  $D$  of  $\sim 10^{-8} \text{ m}^2 \text{ s}^{-1}$ , porosity  $\phi$  of  $\sim 10^{-2}$  (e.g., Fig. 4g), and a very conservative flux  $v_f \phi$  estimate of  $\sim 0.1 \text{ m kyr}^{-1}$  (e.g., Fig. 4h) are used. Adding equation (1) to (2) and (3) to (4) leads to:

$$-(\rho_s - \rho_f) \frac{\partial \phi}{\partial t} + \rho_f \nabla \cdot (\mathbf{v}_f \phi) = \rho_s \mathbf{v}_s \cdot \nabla \phi, \quad (5)$$

$$\frac{\partial[\rho_f \phi c_f^i + \rho_s (1 - \phi) c_s^i]}{\partial t} + \rho_f \nabla \cdot [\phi \mathbf{v}_f c_f^i] + \rho_s \mathbf{v}_s \cdot \nabla [(1 - \phi) c_s^i] = 0. \quad (6)$$

Note that, in deriving equations (5) and (6), the zero-compaction-rate assumption ( $\nabla \cdot \mathbf{v}_s = 0$ ) is used.

In the coordinate system where  $x$ -axis is parallel to and  $z$ -axis is normal to the slab extension, if the angle of flow direction ( $\theta$ ) is uniform across the slab (Fig. 1b), then  $\mathbf{v}_s$  and  $\mathbf{v}_f$  in 2D can be written as:

$$\begin{aligned} \mathbf{v}_s &= (v_s, 0), \\ \mathbf{v}_f &= v_f (\cos \theta, \sin \theta), \end{aligned} \quad (7)$$

where  $v_s$  is the subduction rate,  $v_f$  is the magnitude of fluid velocity, and  $\theta$  is another model parameter that will be explored in section IV. Substituting equation (7) into (5) and (6) yields:

$$-(\rho_s - \rho_f) \frac{\partial \phi}{\partial t} + \rho_f \left[ \cos \theta \frac{\partial (v_f \phi)}{\partial x} + \sin \theta \frac{\partial (v_f \phi)}{\partial z} \right] - \rho_s v_s \frac{\partial \phi}{\partial x} = 0, \quad (8)$$

$$\frac{\partial \bar{c}^i}{\partial t} + \rho_f \cos \theta \frac{\partial (v_f \phi c_f^i)}{\partial x} + \rho_f \sin \theta \frac{\partial (v_f \phi c_f^i)}{\partial z} + \rho_s v_s \frac{\partial}{\partial x} [(1 - \phi) c_s^i] = 0, \quad (9)$$

where  $\bar{c}^i$  is volatile mass per unit rock volume and can be converted to mass fraction via:

$$\bar{c}_{th}^i = \frac{\bar{c}^i}{\rho_f \phi + \rho_s (1 - \phi)}, \quad (10)$$

which is used as input for the thermodynamic module from the companion paper Part I:

$$(\phi, c_s^{H_2O}, c_f^{H_2O}, c_s^{CO_2}, c_f^{CO_2}) = \Phi(P, T, \bar{c}_{th}^{H_2O}, \bar{c}_{th}^{CO_2}). \quad (11)$$

Equations (8)–(11) constitute the governing equations in this study.

The unknowns in the governing equations are the magnitude of fluid velocity ( $v_f$ ), porosity ( $\phi$ ), bulk compositions ( $\bar{c}^i$ ), and  $H_2O$  &  $CO_2$  content in both phases ( $c_f^i, c_s^i$ )—8 unknowns in total. The thermodynamic equation (11) provides solutions to 5 unknowns, so it can be counted as 5 equations. Including equations (8)–(9), the total number of equations is 8, so the set of governing equations is closed. Note that the closedness of governing equations is premised on a chosen flow angle ( $\theta$ ) and on the prescribed steady-state  $P$ – $T$  structure of the slab. To be consistent with the steady-state  $P$ – $T$  field, we also solve the governing equations (8)–(11) until a steady state is reached (after  $\sim 6$  Ma model time for a 5 cm  $yr^{-1}$  convergence rate). Physically, the model can yield the magnitude distribution of fluid velocity with pre-defined uniform flow direction, without resorting to the momentum conservation equation (i.e., Darcy's law). Once the  $P$ – $T$  path of a subducting slab is pre-determined, thermodynamics of local equilibrium dictates the amount of volatiles liberated from or absorbed to every rock parcel during each timestep of the model. Under steady state, if flow direction ( $\theta$ ) is further prescribed, then mass conservation dictates that the magnitude of fluid flux is simply the integration of volatiles released or absorbed (the term  $v_s (\partial \phi / \partial x)$  in equation (8)) along flow trajectories. Readers are referred to Appendix A for further details.

Avoiding the momentum conservation equation in our model has positive and negative consequences. The downside is the lack of emergent dynamic flows; instead, fluid flows are determined by choice of flow direction and conservation of mass along the selected flow paths. As briefly discussed in the introduction, the upside is that the large uncertainties associated with the diversity of possible flow patterns yielded by various dynamic considerations is avoided. For example, two-phase dynamic model using viscous rheology suggests a high-permeability flow channel at the interface between slab and mantle wedge [12], whereas those using visco-elastic rheology show the development of porosity waves within the slab [15]. On smaller spatial scales (e.g., centimeter to meter), Plümper *et al.* [14] and Malvoisin *et al.* [22] show that flow channels and porosity waves can develop as well. Besides, visco-elasto-plastic models suggest that faults formed during slab bending exert a strong control on the fluid flow directions and overall flow pattern within the slab [13]. Indeed, there is vast field evidence attesting to the complexity of fluid flows in subducting slabs [e.g., 23–28]. Designating flow direction ( $\theta$ ) as a free model parameter, however, enables us to approximate the overall trend of fluid flows and explore it by setting  $\theta$  to different values.

In summary, the assumptions regarding the thermo-mechanical aspects of the slab in our model are: (i) rigid plate with a prescribed subduction rate  $v_s$ ; (ii) constant densities for liquid ( $\rho_f$ ) and solid ( $\rho_s$ ) phases; (iii) steady-state  $P$ – $T$  structure of the slab pre-calculated from canonical thermo-mechanical models. The assumptions in the reactive flow model are: (i) local equilibrium between liquid and solid phases; (ii) no diffusion or dispersion of  $H_2O$  and  $CO_2$ ; (iii) flow direction  $\theta$  is prescribed and uniform across the slab; (iv) the reactive flow is solved until a steady state is reached.

TABLE I. Notations of Symbols

Symbol	Meaning	Unit
$D$	diffusion coefficient of CO <sub>2</sub> or H <sub>2</sub> O	$\sim 10^{-8} \text{ m} \cdot \text{s}^{-2}$
$P$	pressure	GPa
$T$	temperature	°C
$H$	slab thickness	m
$i$	H <sub>2</sub> O or CO <sub>2</sub>	
$t$	time	s
$x$	coordinate along slab	m
$z$	coordinate normal to slab	m
$\theta$	uniform flow angle	
$\phi$	porosity	
$\mathbf{v}_f$	fluid velocity	$\text{m} \cdot \text{s}^{-1}$
$v_f$	magnitude of fluid velocity	$\text{m} \cdot \text{s}^{-1}$
$\mathbf{v}_s$	solid velocity	$\text{m} \cdot \text{s}^{-1}$
$v_s$	subduction rate	$\text{m} \cdot \text{s}^{-1}$
$\rho_f$	fluid phase density	$\text{kg} \cdot \text{m}^{-3}$
$\rho_s$	solid phase density	$\text{kg} \cdot \text{m}^{-3}$
$c_f^i$	mass fraction of $i$ in fluid phase	
$c_s^i$	mass fraction of $i$ in solid phase	
$\overline{c^i}$	bulk content of $i$ per unit rock volume	$\text{kg} \cdot \text{m}^{-3}$
$\overline{c_{th}^i}$	bulk mass fraction of $i$	
$\Gamma$	reaction rate	$\text{kg} \cdot \text{m}^{-3} \cdot \text{s}^{-1}$
$\Gamma_i$	reaction rate for $i$	$\text{kg} \cdot \text{m}^{-3} \cdot \text{s}^{-1}$

### III. NUMERICAL METHOD

#### A. Initial and Boundary Conditions

We undertake timestepping for equations (8)–(11) to achieve the steady-state solution. The initial conditions are: bulk volatile content  $\overline{c_{th}^i}$  are uniformly set to those of the incoming rocks on the left boundary; porosity ( $\phi$ ) and volatile content in both phases ( $c_f^i, c_s^i$ ) are determined via the thermodynamic module (eq. (11)); initial fluid speed ( $v_f$ ) is zero across the modelled slab domain.

The incoming slab is assumed to be layered in lithology (Fig. 1b) and thus bulk volatile content:  $c_{th}^{\text{CO}_2} = 3.01 \text{ wt\%}$  and  $c_{th}^{\text{H}_2\text{O}} = 7.29 \text{ wt\%}$  [29] for a sedimentary layer from 0 km to 0.5 km;  $c_{th}^{\text{CO}_2} = 2.95 \text{ wt\%}$  and  $c_{th}^{\text{H}_2\text{O}} = 2.68 \text{ wt\%}$  [7] for a MORB layer from 0.5 km to 2.5 km;  $c_{th}^{\text{CO}_2} = 2.84 \text{ wt\%}$  and  $c_{th}^{\text{H}_2\text{O}} = 2.58 \text{ wt\%}$  [7] for a gabbroic layer from 2.5 km to 6.5 km; and  $c_{th}^{\text{CO}_2} = 0.02 \text{ wt\%}$  and  $c_{th}^{\text{H}_2\text{O}} = 1.00 \text{ wt\%}$  [30] for a slab mantle layer from 6.5 km to 8 km.

As for boundary conditions, since the governing equations are first order in space, no flux ( $v_f = 0$ ) is prescribed for the slab base (Fig. 1b). However, for the ghost points above the upper boundary in the numerical grid, Neumann boundary conditions  $\partial v_f / \partial z$  and  $\partial \overline{c_{th}^i} / \partial z$  are adopted for flow speed and bulk volatile content. The left and right boundary conditions depend on flow direction ( $\theta$ ). When  $\theta \leq 90^\circ$ , the flow paths originate from the left and basal boundaries, so we let  $v_f = 0$  and  $\overline{c_{th}^i} = \overline{c_{th}^i} \Big|_{\text{incoming}}$  on the left, and  $\partial v_f / \partial x = 0$  and  $\partial \overline{c_{th}^i} / \partial x = 0$  on the right. When  $\theta > 90^\circ$ , the flow paths originate from the right and basal boundaries, so we let  $\partial v_f / \partial x = 0$  and  $\partial \overline{c_{th}^i} / \partial x = 0$  on the left, and  $v_f = 0$  and  $\partial \overline{c_{th}^i} / \partial x = 0$  on the right.

#### B. Solution Procedure

The nonlinear character of the governing equations (8)–(11) is evident by inspection. For example, equation (10) shows that bulk volatile content depends on fluid flow ( $v_f, \theta$ ), porosity ( $\phi$ ), and volatile content in each phase ( $c_f^i$ ,

$c_s^i$ ), among which porosity and phase volatile content depend further on bulk compositions through thermodynamics expressed in equation (11). To solve this equation set, we employ the PETSc package [31], following the procedure illustrated in Knepley *et al.* [32] and Katz *et al.* [33] to write down the residual of governing equations (8)–(9). Every timestepping solve is handled by the nonlinear solver provided by PETSc, and the special treatment in our solution procedure is that we emplace the thermodynamic module (eq. (11)) before every evaluation of residuals during Newton iteration.

At the sites where devolatilization onsets, there will be pulses of volatile production owing to the increase of porosity from ideally zero to some finite value determined by thermodynamics. These pulses of volatile production along the envelop of devolatilizing region eventually contribute to integrated volatile fluxes, and cause small fluctuations in the computed fluxes. To focus on the general trend and overall pattern of volatile fluxes within and atop the slab, the results returned by the solution procedure above are post-processed through a smoothing step. Different length scales of smoothing have been experimented with, and we choose 12 numerical grid points (corresponds to 3 km) as the spatial span for smoothing. Details on the smoothing are provided in Appendix A.

#### IV. RESULTS

Before presenting the results for the open-system reference model, we first provide the closed-system results (Fig. 3) with a two-fold goal: firstly to compare our closed-system results with the previous purely thermodynamic model that assumes closed system, and secondly for later comparison with the open-system reference model to elucidate the open-system effects.

##### A. Closed System

The closed system is characterized by the fact that there are no mass fluxes into or out of the rocks of interest, leaving the bulk compositions unaltered. As a result, the bulk  $\text{CO}_2$  &  $\text{H}_2\text{O}$  content of the incoming rocks stay unchanged as subduction proceeds with a speed  $v_s$ ; that is, these bulk values in the slab remain equal to those at the inflow boundary (left side in Fig. 1b). Such a closed-system model corresponds to that typically used in earlier studies, where a representative but fixed bulk composition is used for each rock type to construct thermodynamic pseudosections over which various subduction geotherms are superimposed [34–38].

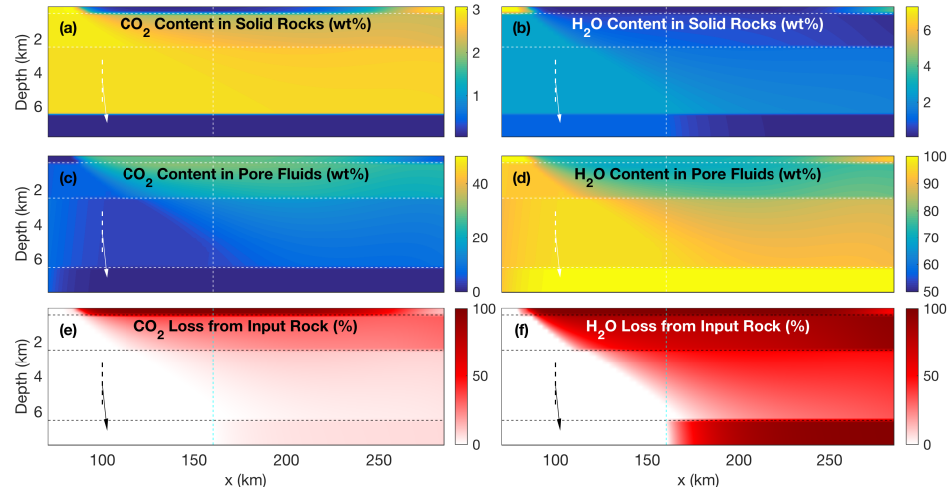


FIG. 3. Results for the closed-system model. Horizontal dashed lines (white or black) mark the lithological interfaces, and long vertical dashed lines mark the position where the basal serpentized upper mantle starts to devolatilize. Divergent colormaps (blue-white-red) are used for panels (e) and (f) where red color corresponds to positive values (volatile loss) and blue color corresponds to negative values (volatile gain). Volatile loss (or gain) in (e) and (f) is calculated relative to its content on the left boundary. Succeeding figures adopt the same line, arrow and color conventions.

With the  $P$ - $T$  field of a hot slab (Fig. 2), Figure 3 shows our closed-system results. Left panels are results on  $\text{CO}_2$ , and right panels on  $\text{H}_2\text{O}$ . From top to bottom, the rows of panels show  $\text{CO}_2$  and  $\text{H}_2\text{O}$  content in the solid rock phase,

liquid volatile phase, and their loss relative to the starting values on the inputting boundary. Of course in a closed system, there should be no volatile loss. However, in closed-system devolatilization models it is conventionally assumed that volatiles, once evolved, are immediately extracted from the bulk system (without altering the bulk composition) [e.g., 34–38]. In this context, a general trend of  $\text{CO}_2$  and  $\text{H}_2\text{O}$  loss from rocks can be seen with along-slab distance in Figure 3a–b, and more clearly in Figure 3e–f. However, there is a reversal of this trend near the slab distance  $\sim 210$  km in the top sedimentary layer (e.g., Fig. 3a). It can also be seen from Figure 3c–d that, within each lithological layer, the coexisting liquid phase is gradually more  $\text{CO}_2$ -rich as subduction goes deeper, except where the trend reversal takes place.

Under the model assumption regarding extraction from a closed-system, the volatile loss in Figure 3e–f is the change in volatile content of the solid phase from its initial value. Since the amount of liquid phase in equilibrium depends on  $P$ – $T$  conditions, the non-uniform  $P$ – $T$  field within the slab yields varying extent of volatile loss in the closed-system model. The trend reversal in Figure 3 can be understood by superimposing the top-layer geotherms over the pseudosection for closed systems [e.g., 37]. The  $P$ – $T$  conditions in the segment beyond  $\sim 210$  km in the top layer exceed the  $P$ – $T$  curve for the onset of devolatilization, but to a lesser extent than the  $P$ – $T$  conditions in the segment before  $\sim 210$  km, leading to a smaller degree of devolatilization.

Depths of volcanic arcs to slab surface range from  $\sim 70$  km to  $\sim 170$  km [39], which correspond to along-slab distances of  $\sim 100$  km to  $\sim 250$  km in Figure 3. Closed-system models predictions, shown in Figure 3a–b and e–f, indicate that slab sediments almost completely lose  $\text{CO}_2$  &  $\text{H}_2\text{O}$  at forearc depths; the basaltic and gabbroic layers can supply significant  $\text{H}_2\text{O}$  but only limited  $\text{CO}_2$  at subarc depths; the slab-mantle lithosphere (serpentinites) can release almost all of its  $\text{H}_2\text{O}$  at subarc depths. All these results compare well with the previous studies that assume closed systems and consider hot subduction geotherms [5–7].

To facilitate later comparison, it is worth noting the implications of the closed-system model for the open-system behaviors in the succeeding sections. Firstly, the basal slab mantle layer in this model contains negligible  $\text{CO}_2$  and serves essentially as a water supplier. Because hydrated slab mantle has only a small set of hydrous minerals (i.e., talc, brucite, serpentine, chlorite),  $\text{H}_2\text{O}$  loss in this layer is more abrupt and complete relative to in basaltic and sedimentary layers. A sudden onset of the supply of the basal  $\text{H}_2\text{O}$  will lead to significant  $\text{H}_2\text{O}$  infiltration in open systems where fluid flow is explicitly considered. Secondly, at the peridotite–gabbro and gabbro–basalt interfaces (6.5 and 2.5 km deep into the slab, respectively), there is a sharp  $\text{CO}_2$  concentration gradient in the liquid phase (Fig. 3c–d). Fluid ascent in the open systems would inevitably cause  $\text{H}_2\text{O}$ -rich and  $\text{CO}_2$ -poor fluid infiltration that enhances decarbonation [8]. Thirdly, the  $\text{CO}_2$  concentration in the liquid phase decreases from the basaltic to the sedimentary layer, suggesting the potential for carbonation by fluid flow down the gradient of  $\text{CO}_2$  concentration.

## B. Open-System Reference Model

Taking all the parameters for the closed-system model above, the reference model additionally considers fluid flows with a uniform direction  $\theta = 90^\circ$  (Fig. 1b), namely, fluid flow is normal to the direction of slab motion ( $\mathbf{v}_s$ ). The results of the steady-state solution to this open-system model are presented in Figure 4. The panel layout of Figure 4 is the same as that of Figure 3 except for the two additional panels in the bottom row. These show the porosity (Fig. 4g) and volatile flux (Fig. 4h) distribution within the slab. To elucidate and further highlight the open-system effects, Figure 5 maps the differences in  $\text{CO}_2$  and  $\text{H}_2\text{O}$  loss (or gain) between the closed- and open-system models, that is, volatile loss in the open system minus that in the closed system. We next consider the reference model results in each layer of the slab, from bottom to top.

The basal slab mantle layer does not experience fluid infiltration because the flows are upward and there is no flux at the bottom boundary. Figure 4c–d shows that the devolatilized liquid phase is almost pure  $\text{H}_2\text{O}$ , given that the inputting peridotitic rock contains negligible bulk  $\text{CO}_2$  (0.02 wt%). Starting from the slab distance  $\sim 160$  km, the  $\text{CO}_2$  loss (Fig. 4e) is small because  $\text{H}_2\text{O}$  tends to be released first during devolatilization, as is pointed out in our companion paper Part I. The  $\text{H}_2\text{O}$  loss is abrupt and complete (Fig. 4f), similar to that for the closed-system model.

On top of the base layer, the gabbro layer is fluxed by nearly pure  $\text{H}_2\text{O}$  sourced from below (Fig. 4c–d). As a result, the infiltration and fractionation effects discussed in Part I come into play. The very  $\text{H}_2\text{O}$ -rich and  $\text{CO}_2$ -poor fluids will infiltrate the base of the gabbro layer, causing enhanced decarbonation and inhibited dehydration. The enhanced  $\text{CO}_2$  loss is evident in Figure 5a, but the expected reduction in  $\text{H}_2\text{O}$  loss is not as clear in Figure 5b. This can be explained by the fractionation effect. Because increased decarbonation reduces the ratio of bulk  $\text{CO}_2$  over  $\text{H}_2\text{O}$ , the onset temperature of devolatilization decreases at the base of the gabbro layer. Given that temperatures within our modelled slab are held fixed, a decrease in the onset temperature would lead to higher extent of devolatilization, offsetting the inhibitive effect on  $\text{H}_2\text{O}$  loss induced by the infiltration. The elevated extent of devolatilization is also reflected by the higher porosity at the base of the gabbro layer in Figure 4g.

The infiltration effect is strongest at the peridotite–gabbro interface because the concentration gradients of  $\text{CO}_2$

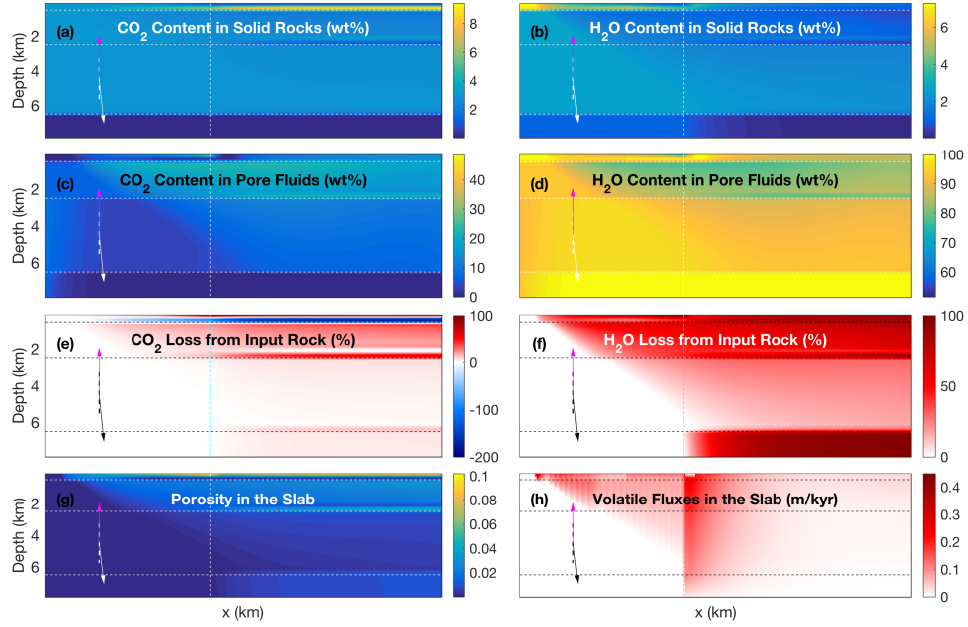


FIG. 4. Results for the open-system reference model. The magenta arrows denote the direction of fluid flow ( $90^\circ$  in the reference model) relative to slab extension, whereas the black or white arrows denote the direction of gravity. The short dashed lines (white or black) are a reference direction normal to the slab extension. Red color in the divergent colormap for volatile flux (panel h) means upward fluid flow, whereas blue color means downward flow. Note the different horizontal and vertical scales in the plots, and the true angle between gravity and the flow direction should be  $145^\circ$ .

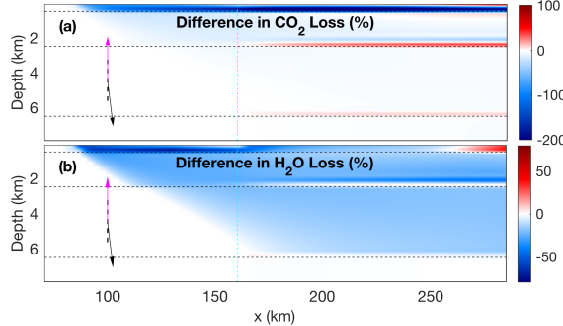


FIG. 5. Differences in  $\text{CO}_2$  and  $\text{H}_2\text{O}$  loss (or gain) between the open- and closed-system models. The difference is calculated by rock  $\text{CO}_2$  or  $\text{H}_2\text{O}$  loss in the open system minus that in the closed system, and percentage values are relative to the initial rock volatile content. Note that, different than those in Figures 3 and 4, red color means enhanced loss or diminished gain, whereas blue color means diminished loss or enhanced gain.

and  $\text{H}_2\text{O}$  in the liquid phase are the steepest (Fig. 4c-d). Above the interface, the liquid phase compositions have been adjusted by the buffering reactions drastically occurring at the interface, so the infiltration effect weakens. In consequence, the bulk interior of the gabbro layer is dominated by the fractionation effect. At and after the onset of devolatilization, preferential  $\text{H}_2\text{O}$  loss causes increased difficulty in devolatilization and thus inhibits overall volatile loss in the bulk interior (Fig. 5).

Further up, the  $\text{H}_2\text{O}$ -rich and  $\text{CO}_2$ -poor fluids (Fig. 4c-d) derived from the gabbro layer infiltrate the base of the basalt layer, similar to the scenario at the base of gabbro layer. Likewise, enhanced  $\text{CO}_2$  loss and approximately unmodified  $\text{H}_2\text{O}$  loss take place at the layer base (Fig. 5), and the overall  $\text{CO}_2$  and  $\text{H}_2\text{O}$  loss is inhibited in the layer interior. The porosity elevation immediately above the gabbro–basalt interface is even more discernible in this case (Fig. 4g). Moreover, elevated porosity levels reflect higher extent of devolatilization. According to our parameterization in the companion paper Part I, higher extent of devolatilization corresponds to higher  $\text{CO}_2$  and

lower H<sub>2</sub>O concentrations in the coexisting liquid phase, which are also evident at  $\sim 2.5$  km depth in Figure 4c–d. Upward infiltration of these fluids, coupled with the fractionation effect, gives rise to the diminished volatile loss immediately above the region of enhanced decarbonation (blue stripes  $\sim 2$  km deep in Fig. 5). Note also that in Figure 5 the degree of decarbonation is higher at the basalt base than at the gabbro base, which is consistent with the higher integrated fluid fluxes at the shallow lithological interface (Fig. 4h).

Figure 4c–d shows that CO<sub>2</sub>-rich and H<sub>2</sub>O-poor fluids will infiltrate at the base of the topmost sedimentary layer. As is inferred from the closed-system model, the infiltration will result in carbonation reactions in the sediments immediately above the lithological contact, which is demonstrated by the negative values of CO<sub>2</sub> loss (i.e., CO<sub>2</sub> gain by the sediments) in Figure 4e. Figure 5a compares the CO<sub>2</sub> loss between the open- and closed-system models; carbon sequestration in the top sedimentary layer is more evident. In Figure 5b, it can be seen that H<sub>2</sub>O loss in the sedimentary layer diminishes before  $\sim 250$  km along the slab coordinate. This is due to the fractionation effect discussed in Part I: carbonation increases the ratio of bulk CO<sub>2</sub> over H<sub>2</sub>O, which further raises the onset temperature of devolatilization and in turn inhibits dehydration. As for the enhanced H<sub>2</sub>O loss after  $\sim 250$  km in Figure 5b, it actually stems from the reversal of trend in the H<sub>2</sub>O loss calculated for the closed-system model (e.g., Fig. 3f).

A common feature above the gabbro–basalt and basalt–sediment interfaces in Figure 5a is the formation of paired stripes of inhibition and enhancement of CO<sub>2</sub> loss, but the stripes in the sedimentary layer are vertically in reverse order to that in the basalt layer. This is because the former is caused by CO<sub>2</sub>-rich fluid infiltration, whereas the latter by H<sub>2</sub>O-rich fluid infiltration. Another noteworthy feature in Figure 5 is that the starting positions of the infiltration-induced stripes in the basalt and gabbro layers coincide horizontally with the onset of dehydration of the slab upper mantle. This coincidence reflects the potential for fluids from hydrated lithospheric mantle to remobilize slab H<sub>2</sub>O and CO<sub>2</sub>. In fact, the enhanced infiltration into the top sedimentary layer causes considerable carbonation that substantially reduces the porosities and fluid fluxes immediately after  $\sim 160$  km along the slab (Fig. 4g–h).

Close examination of Figure 4h suggests that the volatile fluxes fluctuate laterally before the onset of slab mantle dehydration at  $\sim 160$  km. This is because the onset of devolatilization at different slab depths occurs at different horizontal positions that are laterally separated from one another. Since the onset of devolatilization corresponds to a pulse of volatile production, after being vertically integrated into volatile fluxes, these pulses cause the lateral fluctuation in volatile flux distribution. Appendix A discusses this issue further.

### C. Effect of Flow Direction

Different flow trajectories pass through areas with different *P*–*T* conditions that determine different volatile partition coefficients. Hence volatile loss and gain during reactive flow are path-dependent, and we assess the impact of fluid flow direction ( $\theta$ ) on CO<sub>2</sub> and H<sub>2</sub>O fluxes emanating from slab surface. Figure 6 shows the slab surface CO<sub>2</sub> (left panels) and H<sub>2</sub>O (right panels) fluxes with flow angles of 22.5°, 45°, 90°, 135°, and 157.5°. The case of flow angle  $\theta = 90^\circ$  is the open-system reference model already presented in section IV B. Otherwise, all model parameters except the flow angle  $\theta$  are identical to the reference model.

Figure 6 shows profiles of the slab surface volatile flux  $[v_f \phi c_f^i]_{z=0} \sin \theta$ . All the profiles have a peak near  $\sim 80$  km along the slab, caused by the devolatilization of the top sedimentary layer. In addition, there is a dip in all the flux profiles around the starting position of slab-mantle devolatilization ( $\sim 160$  km). This sharp drop of surface flux stems from the boost of carbonation reactions by slab-mantle devolatilization, which reduces the top-layer porosity ( $\phi$ ) and further the surface flux ( $v_f \phi$ ). The shift in position of this dip is due to the change of flow direction that advances ( $\theta > 90^\circ$ ) or retreats ( $\theta < 90^\circ$ ) the carbonation reaction along the slab. A more striking feature in Figure 6 is a second flux peak that emerges at the average position of global arcs, where it projects onto the slab surface (red triangle). As shown in Figure 6g–j, this peak appears only when flow angle  $\theta > 90^\circ$ , that is, for fluid flows that are nearly slab-parallel and up-dip. If it is further assumed that magmas generated by flux melting traverse the mantle wedge vertically without deflection [e.g., 40], Figure 6 implies that up-slab flow is responsible for the magma supply to volcanic arcs.

The emergence of the subarc flux peak in Figure 6 can be explained by Figure 7, which maps the difference in fluxes ( $v_f \phi$ ) between models with flow angle  $\theta \neq 90^\circ$  and the reference model with  $\theta = 90^\circ$ . The flux increase in Figure 7 can be understood by inspecting equation (A2): fluid fluxes accumulate along flow paths and longer paths tend to cause larger fluxes. Moreover, when  $\theta > 90^\circ$ , additional flux increase is caused by flow trajectories tapping into the region of slab-mantle devolatilization (Fig. 7c–d). Conversely, when  $\theta < 90^\circ$ , the flux diminution in Figure 7a–b is caused by flow trajectories passing through regions before the onset of slab mantle devolatilization. As flows with  $\theta > 90^\circ$  can transport more volatiles to slab surface, this explains the emergence of flux peak near  $\sim 150$  km in the flux profiles in Figure 6g–j.

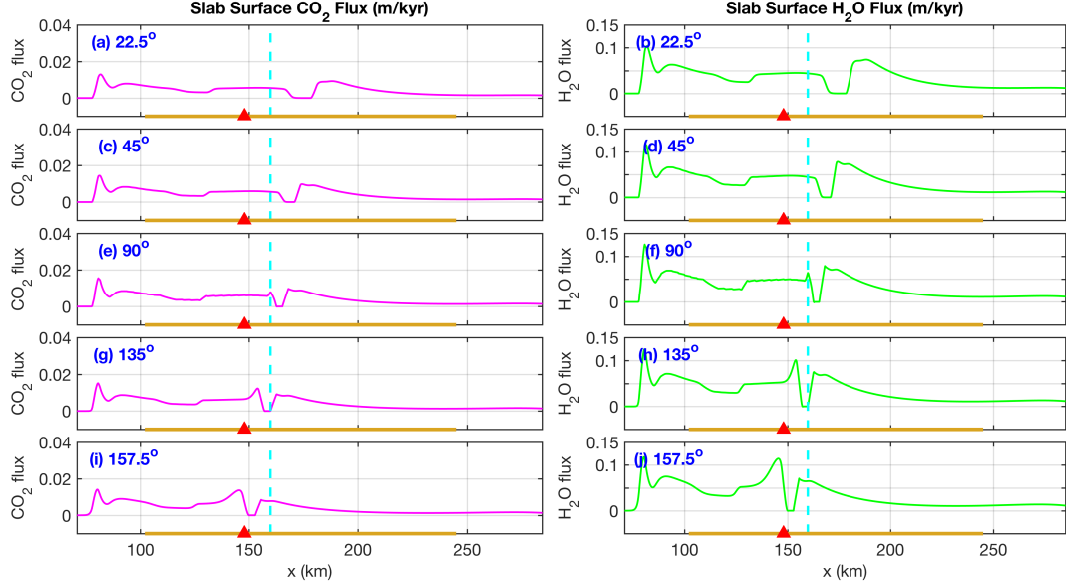


FIG. 6.  $\text{CO}_2$  (left panels) and  $\text{H}_2\text{O}$  (right panels) fluxes along the slab surface as a function of fluid flow direction ( $\theta$ ). Note that the panels (e and f) in the middle row are the fluxes from the reference model in section IV B. Cyan dashed lines mark the starting position of slab mantle devolatilization and this convention applies in the succeeding figures. The solid brown lines draw the global range of arc positions projected onto slab surface [39], and the red triangle marks the site of the average position ( $\sim 150$  km); the same convention is used for following figures.

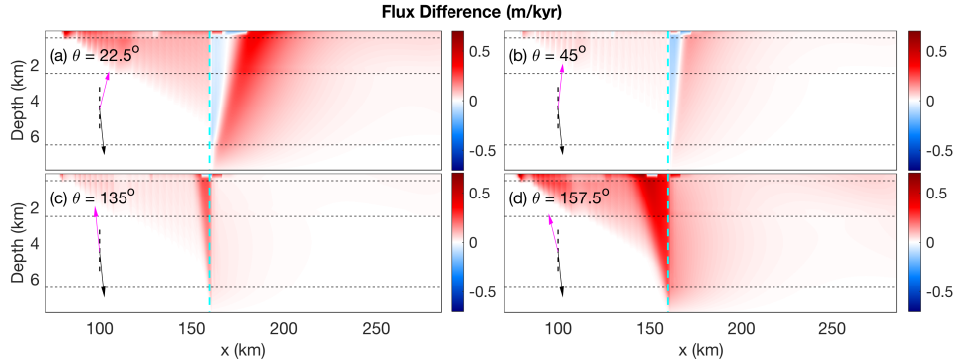


FIG. 7. The difference in fluid fluxes ( $v_f \theta$ ) between the models with flow angle  $\theta \neq 90^\circ$  and the open-system reference model with  $\theta = 90^\circ$ . Red color corresponds to flux increase, and blue color to flux decrease, both relative to the reference model results. Arrows and dashed lines bear the same meaning as in preceding figures. Note that the small patches in the sedimentary layer around  $\sim 160$  km is related to the sharp porosity reduction due to strong carbonation, read the reference model section IV B for more details.

#### D. Effect of Slab Age

Published closed-system and 1D open-system studies [5–8, 37, 38] show that high-temperature subduction geotherms promote slab devolatilization and thus increase slab-surface volatile fluxes. We test this hypothesis using our 2D open-system model. Results with flow angle  $\theta = 90^\circ$  and slab ages ranging from 10 Ma to 60 Ma are shown in Figure 8, where it can be seen that, for old slabs with cold geotherms, devolatilization is deferred to greater depths. For the coldest slab (60 Ma old) in this study, there is almost no dehydration or decarbonation in the range of subarc depths. In general, relative to the reference model with a slab age of 10 Ma, old, cold slabs will release less volatiles around subarc depths, therefore promoting  $\text{CO}_2$  &  $\text{H}_2\text{O}$  recycling into deep mantle [41].

Flow angles in Figure 8 are all  $90^\circ$ , and according to our assessment of the directional effect of flows, it can be inferred that up-slab flows ( $\theta > 90^\circ$ ) will produce flux peaks. However, the positions of these peaks are controlled by the position of the onset of slab-mantle devolatilization. Given that the onset of slab-mantle devolatilization is

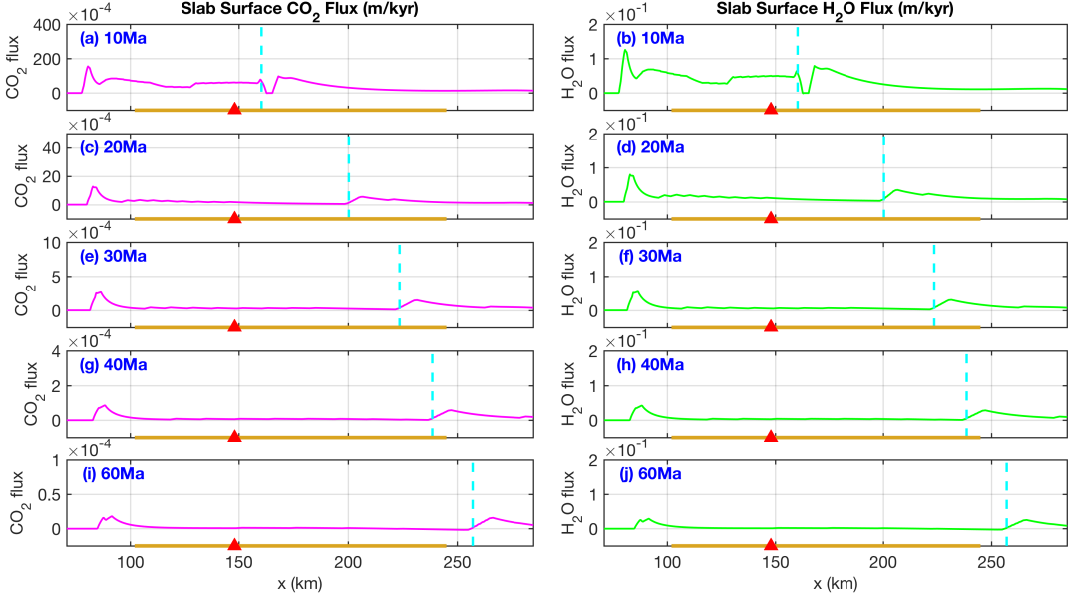


FIG. 8.  $\text{CO}_2$  (left panels) and  $\text{H}_2\text{O}$  (right panels) fluxes along the surfaces of slabs with different ages. The result from the reference model with 10-Ma-old slab is also plotted in the top row for comparison. Note the shift of the position for the onset of slab mantle devolatilization and the flux peak associated with it. Also, note that the  $y$ -axis scales decrease from top row to bottom for  $\text{CO}_2$  fluxes.

also deferred to greater depths in old slabs (Fig. 8), up-slab flows would not affect the subduction efficiency of  $\text{H}_2\text{O}$  and  $\text{CO}_2$  (see section IV G). In other words, cold slabs promote  $\text{H}_2\text{O}$  and  $\text{CO}_2$  recycling even if within-slab flows are upward along the slab.

#### E. Effect of Serpentization

It is commonly proposed that hydration of slab lithospheric mantle takes place at the outer rise of the slab near the trench [42]; subsequent dehydration leads to slab embrittlement, which has been invoked for interpreting subduction zone seismicity [43–46]. Observational seismic studies infer the extent of serpentization to be 5%–31% [47–49], which corresponds to  $\text{H}_2\text{O}$  content of 0.6–3.5 wt% for hydrated slab mantle. Given this uncertainty of  $\text{H}_2\text{O}$  content and its control on the within-slab flux pattern (e.g., Fig. 7), we test how this factor affects slab volatile storage and surface fluxes by varying the  $\text{H}_2\text{O}$  content in the incoming slab mantle lithosphere from 0.5 wt% to 10 wt% (the reference model contains 1 wt%  $\text{H}_2\text{O}$ ). Panels in Figure 9 show the resultant variation of  $\text{CO}_2$  and  $\text{H}_2\text{O}$  fluxes along the slab surface. Firstly, the position of onset for lithosphere devolatilization moves from depth of  $\sim 125$  km to  $\sim 80$  km as the hydration extent of incoming slab increases. This is because increasing bulk  $\text{H}_2\text{O}$  content while keeping bulk  $\text{CO}_2$  constant (negligibly small 0.02 wt%) decreases the onset temperature of devolatilization. Secondly, the magnitudes of slab surface fluxes are substantially increased by the elevated basal  $\text{H}_2\text{O}$  content. Figure 9e–h show that serpentinite dehydration can dominate other controls of slab surface  $\text{CO}_2$  and  $\text{H}_2\text{O}$  fluxes and thus can play a crucial role in arc magmatism and subduction-zone volatile recycling.

In Figure 10, the differences in  $\text{CO}_2$  and  $\text{H}_2\text{O}$  loss relative to that of the reference model are mapped for different hydration states of the slab mantle. For the smaller extent of hydration (Fig. 10a–b), the weakened infiltration leads to general reduction in reaction progress, as demonstrated by the decrease in both the  $\text{CO}_2$  gain at the sites of carbonation (red stripes in Fig. 10a), and the  $\text{CO}_2$  loss at the sites of decarbonation (blue stripe/regions in Fig. 10a). In particular, there is a stripe pair above the basalt–gabbro interface in Figure 10a, but vertically in reverse order to that in Figure 5a. This is still attributable to the diminished infiltration flux as explained above. By contrast, for higher extent of slab mantle hydration (Fig. 10c–f), stripe pairs similar to those in Figure 5a also appear in Figure 10b & e, but are pushed to upper levels due to the increased infiltration flux. Moreover, for very strong infiltration as in Figure 10e, decarbonation is so strong that even the carbonation within the basalt layer is offset (white stripe at  $\sim 2$  km in Fig. 10e). If inspected closely, a red–blue stripe pair appears at the peridotite–gabbro interface at  $\sim 6.5$  km in Figure 10e, which is not the case for the reference model in Figure 5a, and the reason is simply that the stronger

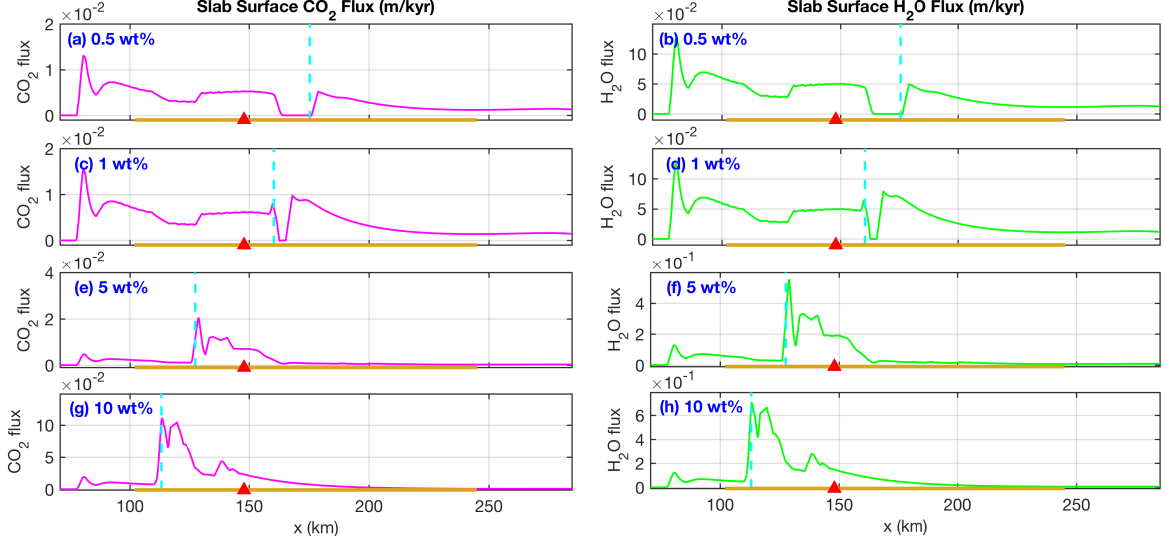


FIG. 9. Slab surface  $\text{CO}_2$  (left panels) and  $\text{H}_2\text{O}$  (right panels) fluxes as a function of initial  $\text{H}_2\text{O}$  content in the basal layer. The reference model (section IV B) contains 1 wt%  $\text{H}_2\text{O}$  and its results are plotted in panels c & d for comparison. The cyan dashed lines mark the onset of dehydration of this basal layer. Note the increase of  $y$ -axis scales in the lower panels.

infiltration makes the stripe pair discernible.

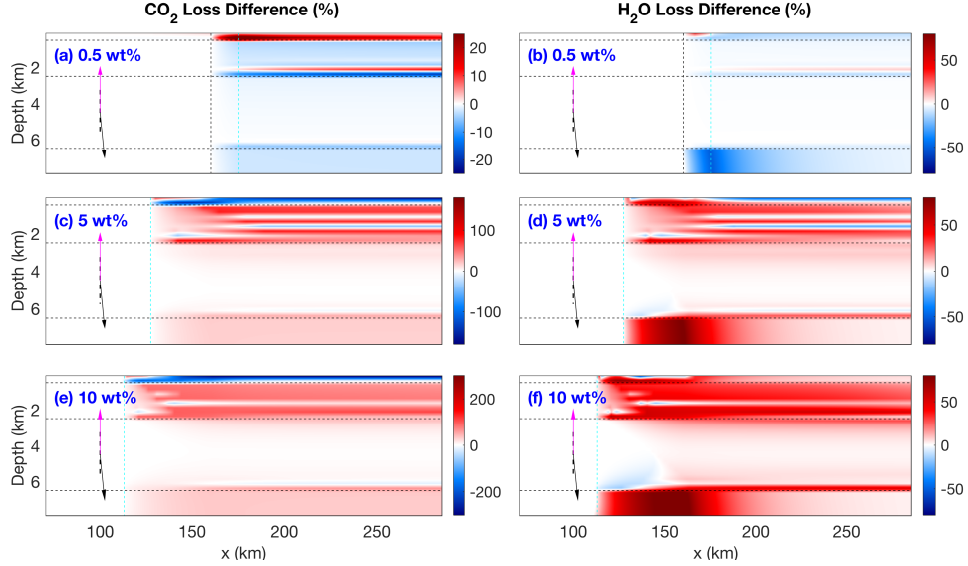


FIG. 10. Differences in  $\text{CO}_2$  (left panels) and  $\text{H}_2\text{O}$  (right panels) loss relative to the reference model, caused by various initial  $\text{H}_2\text{O}$  content in the slab mantle. The percentage values are relative to the initial rock volatile content, as in Figure 5. Red color corresponds to enhanced volatile loss or diminished volatile gain, whereas blue color corresponds to diminished loss or enhanced gain. Note that the thin vertical black dashed lines in (a) and (b) mark the onset of serpentinite dehydration for the reference model, and are plotted here for better comparison.

Quantitatively, for the intensively infiltrated basalt layer in Figure 10c & e,  $\text{CO}_2$  loss can be enhanced to as high as 100%, whereas for the even more intensively infiltrated sedimentary layer, the rise in  $\text{CO}_2$  gain can be as high as 300%. In other words, enhanced infiltration extracts an extra amount of  $\text{CO}_2$  from the gabbro and basalt layers along flow pathways, but much of the extracted  $\text{CO}_2$  is merely redistributed into the top sedimentary layer — only a small fraction escapes the slab surface and contributes to surface fluxes (Fig. 9e & g).

$\text{H}_2\text{O}$  loss or gain differs from that of  $\text{CO}_2$ . For the basalt and gabbro layers, both are infiltrated by  $\text{H}_2\text{O}$ -rich fluids that cause decarbonation above the layer contacts. As illustrated in the companion paper Part I, fractionation

caused by decarbonation leads to a larger extent of overall devolatilization. The enhanced  $\text{H}_2\text{O}$  loss at depths  $\sim 2.5$  km and  $\sim 6.5$  km in Figure 10d & f is a result of this. For the top sedimentary layer, however, it is infiltrated by  $\text{CO}_2$ -rich fluids, so the fractionation caused by carbonation leads to inhibited  $\text{H}_2\text{O}$  loss, as reflected in Figure 10d. Different from that in Figure 10d, the top sedimentary layer in Figure 10f experiences more  $\text{H}_2\text{O}$  loss. This is because the stronger infiltration by  $\text{CO}_2$ -rich fluids also induces dehydration that counteracts the fractionation effect which is dominant for the case in Figure 10d.

#### F. Effect of Sediments Removal by Diapirism

For all of our models so far, a sedimentary layer of 500 m is assumed to cover the slab top and not detach during subduction. However, dynamic study by Behn *et al.* [50] shows that a sedimentary layer  $> 100$  m thick and  $\sim 200 \text{ kg m}^{-3}$  lighter than surrounding peridotites may form rising diapirs that traverse the mantle wedge. Kelemen and Manning [4] proposes that diapirs entraining carbonates are an important avenue for carbon release to mantle lithosphere. We therefore assess the impact of diapirism on slab volatile storage and emission based on a simplified model setup: (i) the topmost 500-m-thick sedimentary layer in the reference model is replaced by basalt of the same composition as the underlying layer, mimicking the scenario of complete removal of sediments; (ii) fluid flow angles are varied among  $22.5^\circ, 45^\circ, 90^\circ, 135^\circ, 157.5^\circ$  to examine the resultant slab surface fluxes.

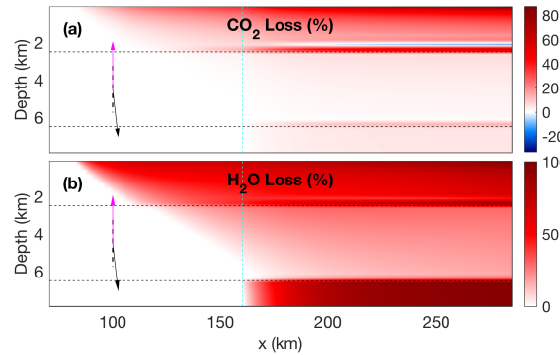


FIG. 11. Volatile loss for the three-layer slab model, that is, there is no capping sedimentary layer on the slab surface due to diapiric removal.

For the three-layer model with a  $90^\circ$  flow angle, Figure 11 maps the volatile loss within the slab. Regarding  $\text{CO}_2$  loss (Fig. 11a), except for the thin sheet of  $\text{CO}_2$  gain above the basalt–gabbro interface, the entire plate loses  $\text{CO}_2$ , and the loss can reach a maximum of 60% on the surface of the basalt layer. The thin sliver of up to 25%  $\text{CO}_2$  gain is due to the infiltration-related carbonation, as previously explained. In contrast,  $\text{H}_2\text{O}$  loss in Figure 11b is similar to that of the reference model. This is because the sedimentary layer, even if it survives diapirism, should dehydrate and not restrict  $\text{H}_2\text{O}$  transport from beneath.

Figure 12 provides the  $\text{CO}_2$  and  $\text{H}_2\text{O}$  slab-surface volatile flux profiles for the three-layer model with the various flow angles ( $\theta$ ). Figure 12 shows that diapiric removal of the capping sediments leads to an overall increase of the  $\text{CO}_2$  fluxes, and additionally to the emergence of a broad flux peak at subarc depths. In particular, when fluid flow is nearly up-slab (Fig. 12k & l), the depth of the flux peak coincides with the average depth of global arc volcanoes projected onto slab surface [39]. It is also interesting to compare between the flux profiles of the four-layer (Fig. 12a) and three-layer models (Fig. 12g), both with a flow angle of  $90^\circ$ : the carbonation reaction in the sedimentary layer clearly suppresses the  $\text{CO}_2$  flux peak that would appear without it. Up-slab flows ( $\theta > 90^\circ$ ) can therefore avoid the more reactive sediments at greater depths, and eventually contribute to slab surface  $\text{CO}_2$  fluxes. On the other hand, removal of the capping sediments does not increase the slab surface  $\text{H}_2\text{O}$  fluxes, except that it removes the flux dip at  $\sim 160$  km in the four-layer reference model (Fig. 12b). It is clear from our analysis of the open-system reference model (section IV B) that the flux dip stems from porosity reduction due to enhanced carbonation in the sedimentary layer, thus the dip is eliminated after the removal of the sedimentary layer.

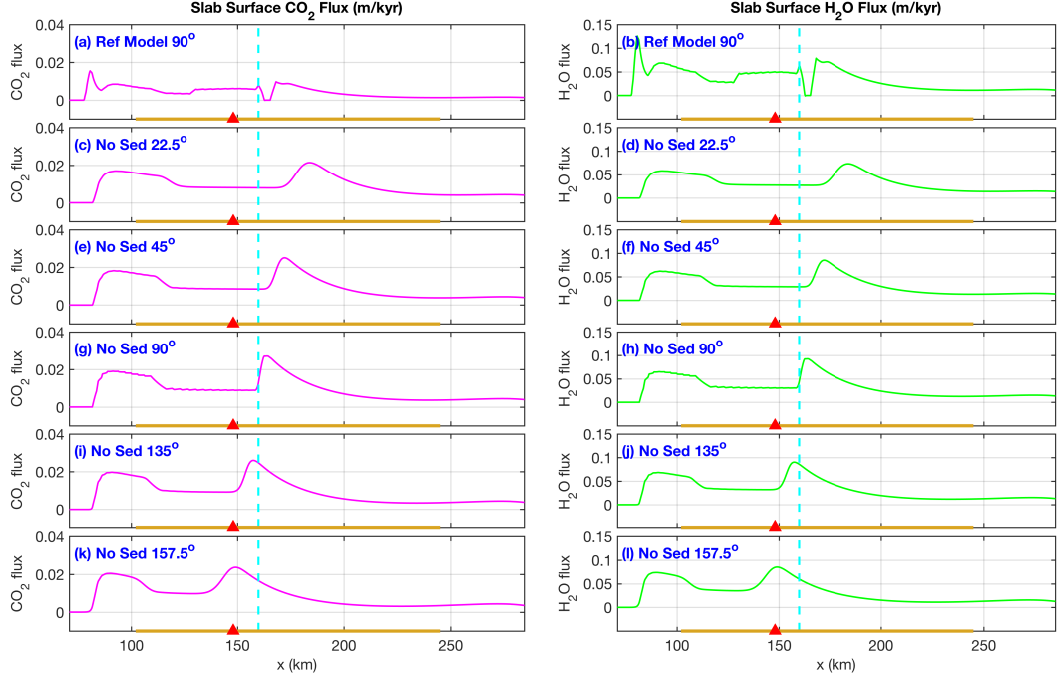


FIG. 12.  $\text{CO}_2$  (left panels) and  $\text{H}_2\text{O}$  (right panels) fluxes on the slab surface. Panels (a) and (b) are from the reference model that has a 500-m-thick sedimentary layer atop the slab, whereas the rest are results from the three-layer model with different flow angles ( $\theta$ ).

#### G. Subduction Efficiency of $\text{H}_2\text{O}$ and $\text{CO}_2$

The subduction efficiency of  $\text{H}_2\text{O}$  (or  $\text{CO}_2$ ) in this study is defined as the quotient of its total mass residing in the solid rock phase beyond  $\sim 200$  km deep over that residing in the incoming slab. To demonstrate how the various factors in the preceding sections affect the subduction efficiency, we plot them in Figure 13.

Both Figure 13a and b suggest that the direction of flow exerts almost no influence on the volatile subduction efficiency. Comparison between the open-system results in Figure 13a and b indicates that the subduction efficiency of  $\text{CO}_2$  is reduced by  $\sim 11\%$ , due to the elimination of carbon sequestration associated with the sedimentary layer. Figure 13c illustrates that slab age strongly influences volatile subduction efficiency—the older the slab, the higher the efficiency. In particular, the 60-Ma-old cold slab is nearly 100% and 93% efficient in recycling  $\text{CO}_2$  and  $\text{H}_2\text{O}$  beyond mantle depth of  $\sim 200$  km. In addition, Figure 13d shows that the  $\text{H}_2\text{O}$  content of hydrated slab mantle exerts much stronger control on the efficiency of volatile subduction. For extensively hydrated slab mantle (e.g., 10 wt%  $\text{H}_2\text{O}$ ), the recycling efficiency of  $\text{CO}_2$  can be reduced to  $\sim 80\%$  and that of  $\text{H}_2\text{O}$  to as low as  $\sim 21\%$ .

Given that reactive flows are path-dependent, the finding that the subduction efficiency in Figure 13a and b is insensitive to flow direction is surprising. However, it can be understood from the two assumptions in the model. The first is the local equilibrium assumption, which dictates that, as long as the  $P$ - $T$  structure of the slab is constant, steady-state volatile production within the entire slab is determined by  $\rho_s v_s \partial\phi/\partial z$  (see Appendix A). Since porosity  $\phi$  further depends on bulk composition, which is affected by flow directions, in theory the volatile production ( $\rho_s v_s \partial\phi/\partial z$ ) should be path-dependent and thereby give rise to path-dependence of subduction efficiency. However, changes in bulk  $\text{H}_2\text{O}$  and  $\text{CO}_2$  content induced by varying flow direction are small and spatially limited such that the path-dependence of subduction efficiency becomes indiscernible in Figure 13a and b. Thus, the flow angle ( $\theta$ ) shifts the volatile flux peaks, but not the overall amount of devolatilization. The second relevant model assumption is the uniform flow direction across slab, which makes strongly focused flows unlikely and hence prevents substantial alternations of bulk volatile content.

The subduction efficiency of  $\text{H}_2\text{O}$  has also been estimated by previous studies that don't consider  $\text{CO}_2$ . For example, van Keken *et al.* [37] estimate an average subduction efficiency of 32% for  $\text{H}_2\text{O}$  in the present-day subducting slabs. In their model, the basal slab-mantle layer is 4 km thick and contains 2 wt%  $\text{H}_2\text{O}$ . In terms of the total amount of  $\text{H}_2\text{O}$  infiltration, this is roughly equivalent to a  $\text{H}_2\text{O}$  content of 5.3 wt% in the 1.5 km thick basal layer in our model. As shown in Figure 13d, our model yields a  $\text{H}_2\text{O}$  subduction efficiency of  $\sim 35\%$ . Nonetheless, the average slab age in

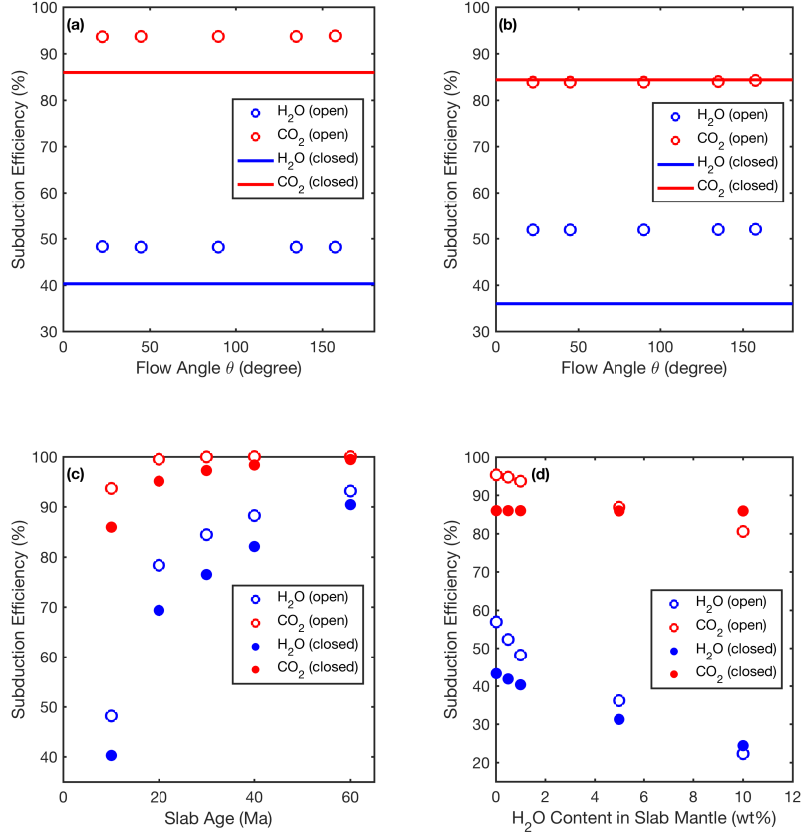


FIG. 13. Subduction efficiency of  $\text{H}_2\text{O}$  (blue) and  $\text{CO}_2$  (red). (a) Effect of flow angle  $\theta$ , results extracted from section IV B and IV C. The closed-system subduction efficiencies do not depend on flow directions, so are plotted as lines. (b) Effect of flow angle  $\theta$ , results extracted from the model without the top sedimentary layer in section IV F. Same as in (a), the horizontal lines denote closed-system efficiencies. (c) Effect of slab age, results extracted from section IV D. Open circles denote open-system results, whereas dots denote closed-system ones; same markers in (d). (d) Effect of the  $\text{H}_2\text{O}$  content in the hydrated slab upper mantle, results extracted from section IV E.

the model by van Keken *et al.* [37] is older than 10 Ma that is adopted in the calculation for Figure 13d, implying that our model would yield a  $\text{H}_2\text{O}$  subduction efficiency higher than 35% for the present-day global subduction zones. The higher subduction efficiency of  $\text{H}_2\text{O}$  is expected because our model accounts for open-system effects. As demonstrated in Figure 13, the subduction efficiency of  $\text{H}_2\text{O}$  is generally lower in closed-system models than in open-system ones. This is mainly due to the fractionation-induced inhibition of  $\text{H}_2\text{O}$  loss in the bulk interior of subducted lithological layers (see section IV B). Only in the case of strong infiltration in Figure 13d does the  $\text{H}_2\text{O}$  (and  $\text{CO}_2$ ) subduction efficiency become lower in open systems than in closed systems. Similar to  $\text{H}_2\text{O}$ ,  $\text{CO}_2$  subduction efficiency is also elevated by open-system fractionation (Fig. 13a, c, d); but for the case without the top sedimentary layer, the open-system models yield comparable efficiencies to the closed-system one, indicating that the fractionation has a stronger influence on  $\text{H}_2\text{O}$  recycling than on  $\text{CO}_2$ . Moreover, comparison between Figure 13a and b suggests that, for closed systems, removal of top sedimentary layer exerts almost no effect on the  $\text{CO}_2$  subduction efficiency; however, for open systems, the  $\text{CO}_2$  subduction efficiency is reduced by  $\sim 10\%$  due to the sediment removal, highlighting again the importance of open-system effects.

## V. DISCUSSION

By treating the subducting slab as a non-deformable plate and assuming local equilibrium and uniform flow direction, our model solves for the steady-state reactive flows of  $\text{H}_2\text{O}$  and  $\text{CO}_2$  and quantifies their fluxes from and storage within the slab. The merit of the model is its capability to couple open-system thermodynamics with fluid flow in a more realistic and consistent way. However, in achieving this capability, the choices made in model setup also impose limitations.

The first limitation lies in neglecting partial melting. Various studies have focused on the effects of merely  $\text{H}_2\text{O}$  on partial melting, and suggest that melting primarily occurs in the overlying mantle wedge due to solidus depression caused by slab-derived  $\text{H}_2\text{O}$  [40, 51]. Field studies in volcanic arc settings, however, discovered adakites that are interpreted to be evidence of slab melting in hot geotherms [52, 53]. When  $\text{CO}_2$  is taken into account, experimental studies suggest that even in hot subduction zones, modern slab geotherms are still below the solidi of carbonated basalts and peridotites, and that only carbonated sediments are promising for carbonatite liberation [1, and references therein]. In light of these experimental findings, neglect of the partial melting of basalt, gabbro, and slab mantle peridotite in our model is a reasonable choice, but ignoring the melting of the sedimentary layer would overestimate the subduction efficiency of  $\text{CO}_2$ , given that migration of carbonatitic melt can remove considerable  $\text{CO}_2$  from the slab.

The second limitation is the omission of aqueous ionic species in the liquid phase in our model. Ionic carbon species other than molecular form (e.g.,  $\text{CO}_2$ ,  $\text{CH}_4$ , etc.) are inferred to be common in subduction zone settings from field studies [e.g., 9, 54]. However, recent detailed thermodynamic modelling by Connolly and Galvez [11] suggests that molecular carbon species might dominate over ionic ones in fluids derived from subducted sediments. The same study also shows that potassium in ionic form can be depleted from the slab-top sediments, destabilizing hydrous phases like micas and thus facilitating volatile release. In light of this, omission of the contribution from aqueous ionic species in the thermodynamics of our model might underestimate the  $\text{H}_2\text{O}$  and  $\text{CO}_2$  fluxes from the slab and in turn overestimate their recycling efficiency.

The third limitation arises from the assumption of uniform flow directions. As explained in section II on the model setup, choosing the flow direction  $\theta$  as a free parameter enables the model to explore the variation of general patterns of within-slab flows predicted by various dynamic models; however, it suffers from losing the details of flow dynamics within the slab. In particular, the strong flow focusing, widely documented in the field [e.g., 23–25, 27], and predicted by dynamic models [e.g., 12–14, 22], cannot be simulated in the current model. As demonstrated by Wada *et al.* [55], heterogeneous hydration associated with local flow focusing can promote  $\text{H}_2\text{O}$  release and reduce its subduction efficiency. Therefore, further work remains to incorporate dynamics into the open-system flow model to evaluate how flow focusing can affect the slab-surface fluxes of  $\text{CO}_2$  and  $\text{H}_2\text{O}$ , and their recycling efficiency by subduction.

The fourth limitation relates to the assumption of no compaction in the slab. To assess the effect of compaction, we compare the magnitude of fluid fluxes in our reference model with that in the compaction model by Wilson *et al.* [12]. Our slab model (section IV B) initially contains  $\sim 2.60$  wt%  $\text{H}_2\text{O}$  on average, yielding a maximum surface flux of  $\sim 0.1 \text{ m kyr}^{-1}$  (Fig. 6f). In contrast, the compaction model initially contains  $\sim 1.85$  wt%  $\text{H}_2\text{O}$  on average, yielding a maximum surface flux of  $\sim 0.8 \text{ m kyr}^{-1}$ . Taken at face value, the compaction model generates a flux that is eight times larger than that from our non-compaction model. However, as shown in Figure 5b, the  $\text{H}_2\text{O}$  flux drop in our reference model is caused not only by neglecting compaction, but also by the open-system fractionation, which can account for up to  $\sim 70\%$  of the flux drop. If this open-system effect were considered by Wilson *et al.* [12], the magnitude of  $\text{H}_2\text{O}$  fluxes in their model would become comparable to that in our reference model, indicating that the influence of compaction is insignificant with respect to the magnitude of slab surface fluxes.

In interpreting our model results on the slab surface fluxes, an additional assumption is made that magmas produced by flux melting of the mantle wedge traverse the wedge vertically without any lateral deflection to feed arc volcanoes. It follows that, if the average position of global arc volcanoes is projected downwards onto the slab surface, it should correspond to a peak in slab surface flux. It is under this assumption that the up-slab flows in Figure 6 are necessary to produce the melt feeding arc volcanism. However, two-phase geodynamic models of the mantle wedge suggest that the melt and fluid transport through the wedge is more complex than simply vertical, and depends on many factors including solid rheology and grain size in the wedge [12, 56, 57]. In addition, the coincidence of flux peaks and the projected volcanic arc position in Figure 6 and 12 is premised on the hot thermal structure of the 10-Ma-old slab. As demonstrated in Figure 8 and 9, old slab shifts the flux peak to greater depths, and higher hydration extent of slab base shifts the peak to shallower depths. Since slower convergence rate leads to a warmer subducting slab [58], it can be expected that the position of flux peak also varies with convergence rate. How the shift in flux peak position influences the dynamics of melt or volatile transport in the wedge, and eventually the genesis of arc magmas, remains to be explored by future models that include both the dynamics and thermodynamics in the wedge.

## VI. CONCLUSION

In summary, we assess the controlling factors for  $\text{CO}_2$  and  $\text{H}_2\text{O}$  release from subducting slabs. We find that up-slab flows are necessary to form a flux peak at subarc depths, which could be responsible for the magmatic genesis of arc volcanoes if the flux-induced melts traverse the mantle wedge vertically. Sufficiently hydrated slab mantle can relax the above requirement for flow directions, but when the slab mantle is additionally carbonated, the onset position of its devolatilization becomes deeper, still making up-slab flows important for supplying maximum volatile release at subarc depths. Moreover,  $\text{H}_2\text{O}$  infiltration from dehydrating slab mantle can mobilize  $\text{CO}_2$  in the overlying gabbroic and basaltic layers, but only redistribute the carbon to the slab surface sediments where significant carbonation takes place. The subducting sediments, if surviving diapiric removal and partial melting, can be an important barrier to  $\text{CO}_2$  liberation from slabs. Conversely, diapirism and partial melting of the sediments can be crucial avenues for  $\text{CO}_2$  transfer from subducting slab to mantle wedge. The subduction efficiency of  $\text{H}_2\text{O}$  is  $\sim 20\%-90\%$  in our model, generally higher than that in previous closed-system models that consider only  $\text{H}_2\text{O}$ . The  $\text{CO}_2$  subduction efficiency is  $\sim 80\%-100\%$ , indicating that a considerable fraction of subducted  $\text{CO}_2$  goes beyond  $\sim 200$  km into deeper mantle. The high subduction efficiency of volatiles in our model stems from the open-system fractionation effect that inhibits overall devolatilization in the interiors of lithological layers. It is probably an overestimate because the effects of flow focusing and ionic carbon dissolution are ignored in the model, which should be explored in future studies. The flow focusing effect can be investigated with the simple parameterization we developed in the companion paper Part I, whereas assessment of the ionic species effect requires a more refined parameterization that considers all possible ions in the liquid phase.

## Appendix A: Appendix

At steady state, the fluid fluxes can be calculated according to equation (5) that further reduces to:

$$\rho_f \nabla \cdot (\mathbf{v}_f \phi) = \rho_s \mathbf{v}_s \cdot \nabla \phi. \quad (\text{A1})$$

Figure 14 shows part of the numerical grid established on the slab coordinate system (Fig. 1b), where the fluid fluxes  $F = v_f \phi$  can then be expressed through integration along flow path ( $l$ ):

$$F = \int_{\text{path start}}^{\text{path end}} \frac{\rho_s}{\rho_f} v_s \frac{\partial \phi}{\partial x} \, dl. \quad (\text{A2})$$

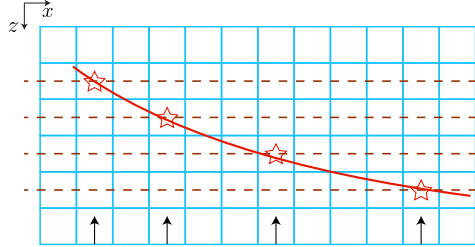


FIG. 14. An illustrative part of the numerical grid in this study. Stars mark the position where onset of devolatilization occurs at relevant slab depths, and the connecting red solid line is the envelope for devolatilization onset within the slab. Brown dashed lines are iso-depth traverses along which  $\partial\phi/\partial x$  will be plotted in Figure 15a, and black arrows denote the direction of flux integration for the reference model ( $\theta=90^\circ$ ).

For the reference model with flow direction  $\theta = 90^\circ$ , flow paths are perpendicular to the slab, so the integration is along the  $z$ -axis direction in Figure 14. At any specific depth (dashed lines in Fig. 14), the onset of devolatilization leads to an abrupt elevation of porosity ( $\phi$ ) and thus a pulse in the  $\partial\phi/\partial x$  profile along the iso-depth traverse. Figure 15 shows the  $\partial\phi/\partial x$  and flux profiles along various iso-depth traverses within the modelled slab, and Figure 15a illustrates that the pulses in  $\partial\phi/\partial x$  appear at different horizontal positions in the slab. According to equation (A1), when flow trajectories pass the locations of the pulses, the calculated fluid fluxes will inherit these pulses. For the reference model where flow paths are normal to  $x$ -axis and the pulses are horizontally apart from one another (Fig. 14), the inherited pulses lead to the fluctuation in the fluid flux distribution (Fig. 15b–c and Fig. 4g). Beyond the slab distance  $\sim 160$  km where the basal slab mantle dehydrates, the envelope of the onset of devolatilization (red solid

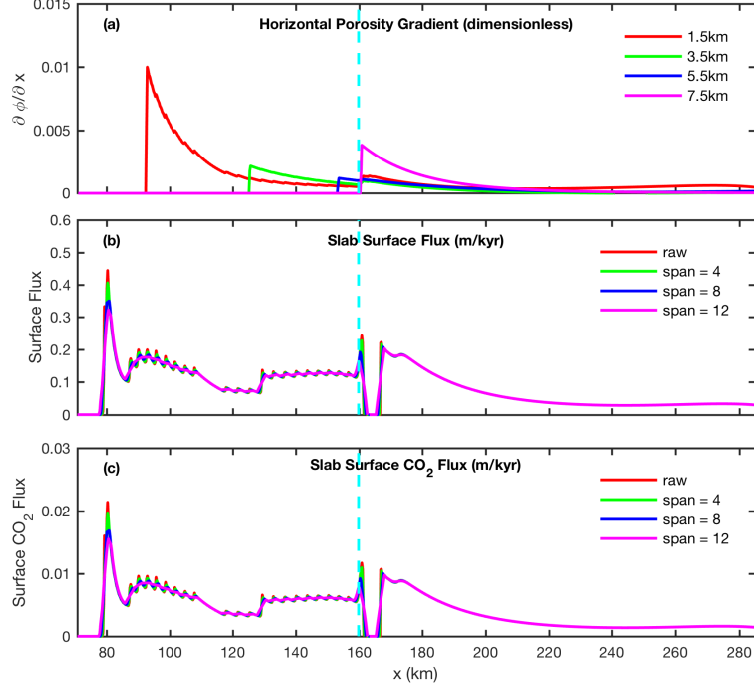


FIG. 15. (a). Profiles of  $\partial\phi/\partial x$  that contributes to fluid fluxes. Different line colors are used to distinguish the depths at which these profiles are extracted from the open-system reference model in section IV B. (b). Slab surface fluxes from the reference model. Red line denotes the raw model result that shows flux fluctuations, whereas other lines represent the model result smoothed to different extent. The “span” here means the number of neighboring grid points used for averaging the flux at a specific grid point. The spacing between grid points in the model is 250 m, so a span of 12 corresponds to an averaging window width of 3 km. (c). Same as in (b), but is for slab surface  $\text{CO}_2$  flux. Vertical dashed lines mark the onset of dehydration for slab lithospheric mantle.

line in Fig. 14) is surpassed, so there are no pulses in  $\partial\phi/\partial x$  at any depth. The flux fluctuations disappear accordingly as in Figure 15b–c and Figure 4h.

The analysis above indicates that refining numerical grid will produce more but weaker fluctuations in slab surface fluxes before  $\sim 160$  km, but the trend and main features of flux profiles stay unchanged. To focus on the general trend and main features, we smooth the flux profiles by averaging over a span of neighboring grid points. As illustrated in Figure 15b–c, smoothing with a span of 12 grid points (3 km) well preserves the flux trend and features, so it is applied to all the slab surface flux profiles in this study.

## ACKNOWLEDGMENTS

The authors thank the Isaac Newton Institute for Mathematical Sciences for holding the Melt in the Mantle program sponsored by EPSRC Grant Number EP/K032208/1. Support from Deep Carbon Observatory funded by the Sloan Foundation is acknowledged. M.T. acknowledges the Royal Society Newton International Fellowship (NF150745). D.R.J acknowledges research funding through the NERC Consortium grant NE/M000427/1 and NERC Standard grant NE/I026995/1. This contribution is about numerical modelling, so it does not depend on experimental or field data. Relevant data and equations for reproducing the model results are already contained in the text. Nonetheless, we provide an example code on the usage of the thermodynamic parameterization: [https://bitbucket.org/mengtian/example\\_code\\_thermo\\_module/src/master/](https://bitbucket.org/mengtian/example_code_thermo_module/src/master/).

---

[1] R. Dasgupta, R. M. Hazen, A. P. Jones, and J. A. Baross, Ingassing, storage, and outgassing of terrestrial carbon through geologic time, *Rev. Mineral. Geochem.* **75**, 183 (2013).

[2] R. Dasgupta and M. M. Hirschmann, The deep carbon cycle and melting in Earth's interior, *Earth Planet. Sci. Lett.* **298**, 1 (2010).

[3] M. M. Hirschmann, Comparative deep Earth volatile cycles: the case for c recycling from exosphere/mantle fractionation of major ( $H_2O$ , C, N) volatiles and from  $H_2O/Ce$ ,  $CO_2/Ba$ , and  $CO_2/Nb$  exosphere ratios, *Earth Planet. Sci. Lett.* **502**, 262 (2018).

[4] P. B. Kelemen and C. E. Manning, Reevaluating carbon fluxes in subduction zones, what goes down, mostly comes up, *Proc. Natl. Acad. Sci. U. S. A.* **112**, E3997 (2015).

[5] D. M. Kerrick and J. A. D. Connolly, Subduction of ophiocarbonates and recycling of  $CO_2$  and  $H_2O$ , *Geology* **26**, 375 (1998).

[6] D. M. Kerrick and J. A. D. Connolly, Metamorphic devolatilization of subducted marine sediments and the transport of volatiles into the Earth's mantle, *Nature* **411**, 293 (2001).

[7] D. M. Kerrick and J. A. D. Connolly, Metamorphic devolatilization of subducted oceanic metabasalts: implications for seismicity, arc magmatism and volatile recycling, *Earth Planet. Sci. Lett.* **189**, 19 (2001).

[8] P. J. Gorman, D. M. Kerrick, and J. A. D. Connolly, Modeling open system metamorphic decarbonation of subducting slabs, *Geochem. Geophys. Geosyst.* **7**, 10.1029/2005GC001125 (2006).

[9] J. J. Ague and S. Nicolescu, Carbon dioxide released from subduction zones by fluid-mediated reactions, *Nat. Geosci.* **7**, 355 (2014).

[10] D. A. Sverjensky, V. Stagno, and F. Huang, Important role for organic carbon in subduction-zone fluids in the deep carbon cycle, *Nat. Geosci.* **7**, 909 (2014).

[11] J. A. D. Connolly and M. E. Galvez, Electrolytic fluid speciation by Gibbs energy minimization and implications for subduction zone mass transfer, *Earth Planet. Sci. Lett.* **501**, 90 (2018).

[12] C. R. Wilson, M. Spiegelman, P. E. van Keken, and B. R. Hacker, Fluid flow in subduction zones: The role of solid rheology and compaction pressure, *Earth Planet. Sci. Lett.* **401**, 261 (2014).

[13] M. Faccenda, T. V. Gerya, and L. Burlini, Deep slab hydration induced by bending-related variations in tectonic pressure, *Nat. Geosci.* **2**, 790 (2009).

[14] O. Plümper, T. John, Y. Y. Podladchikov, J. C. Vrijmoed, and M. Scambelluri, Fluid escape from subduction zones controlled by channel-forming reactive porosity, *Nat. Geosci.* **10**, 150 (2017).

[15] M. Morishige and P. E. van Keken, Fluid migration in a subducting viscoelastic slab, *Geochem. Geophys. Geosyst.* **19**, 337 (2018).

[16] P. E. van Keken, C. Currie, S. D. King, M. D. Behn, A. Cagnioncle, J. He, R. F. Katz, S.-C. Lin, E. M. Parmentier, M. Spiegelman, and K. Wang, A community benchmark for subduction zone modeling, *Phys. Earth Planet. Inter.* **171**, 187 (2008).

[17] P. C. England and R. F. Katz, Melting above the anhydrous solidus controls the location of volcanic arcs, *Nature* **467**, 700 (2010).

[18] D. McKenzie, The generation and compaction of partially molten rock, *J. Petrol.* **25**, 713 (1984).

[19] D. R. Scott and D. J. Stevenson, Magma ascent by porous flow, *J. Geophys. Res.-Solid Earth* **91**, 9283 (1986).

[20] R. F. Katz, Magma dynamics with the enthalpy method: Benchmark solutions and magmatic focusing at mid-ocean ridges, *J. Petrol.* **49**, 2099 (2008).

[21] T. Keller and R. F. Katz, The role of volatiles in reactive melt transport in the asthenosphere, *J. Petrol.* **57**, 1073 (2016).

[22] B. Malvoisin, Y. Y. Podladchikov, and J. C. Vrijmoed, Coupling changes in densities and porosity to fluid pressure variations in reactive porous fluid flow: Local thermodynamic equilibrium, *Geochem. Geophys. Geosyst.* **16**, 4362 (2015).

[23] J. J. Ague, Models of permeability contrasts in subduction zone melange: Implications for gradients in fluid fluxes, syros and tinos islands, greece, *Chem. Geol.* **239**, 217 (2007).

[24] P. Philippot and J. Selverstone, Trace-element-rich brines in eclogitic veins: implications for fluid composition and transport during subduction, *Contrib. Mineral. Petrol.* **106**, 417 (1991).

[25] A. C. Barnicoat and I. Cartwright, Focused-flow during subduction: oxygen isotope data from high-pressure ophiolites of

the Western Alps, *Earth Planet. Sci. Lett.* **132**, 53 (1995).

[26] B. Putlitz, A. Matthews, and J. W. Valley, Oxygen and hydrogen isotope study of high-pressure metagabbros and metabasalts (Cyclades, Greece): implications for the subduction of oceanic crust, *Contrib. Mineral. Petro.* **138**, 114 (2000).

[27] C. M. Breeding, J. J. Ague, M. Brocker, and E. W. Bolton, Blueschist preservation in a retrograded, high-pressure, low-temperature metamorphic terrane, Tinos, Greece: implications for fluid flow paths in subduction zones, *Geochim. Geophys. Geosyst.* **4**, 10.1029/2002GC000380 (2003).

[28] C. M. Breeding, J. J. Ague, and M. Bröcker, Fluid-metasedimentary rock interactions in subduction-zone mélange: implications for the chemical composition of arc magmas, *Geology* **32**, 1041 (2004).

[29] T. Plank and C. H. Langmuir, The chemical composition of subducting sediment and its consequences for the crust and mantle, *Chem. Geol.* **145**, 325 (1998).

[30] S. R. Hart and A. Zindler, In search of a bulk-Earth composition, *Chem. Geol.* **57**, 247 (1986).

[31] S. Balay, S. Abhyankar, M. F. Adams, J. Brown, P. Brune, K. Buschelman, L. Dalcin, A. Dener, V. Eijkhout, W. D. Gropp, D. Kaushik, M. G. Knepley, D. A. May, L. C. McInnes, R. T. Mills, T. Munson, K. Rupp, P. Sanan, B. F. Smith, S. Zampini, H. Zhang, and H. Zhang, PETSc Web page, <http://www.mcs.anl.gov/petsc> (2018).

[32] M. G. Knepley, R. F. Katz, and B. Smith, Developing a geodynamics simulator with petsc, in *Numerical Solution of Partial Differential Equations on Parallel Computers* (Springer, 2006) pp. 413–438.

[33] R. F. Katz, M. G. Knepley, B. Smith, M. Spiegelman, and E. T. Coon, Numerical simulation of geodynamic processes with the portable extensible toolkit for scientific computation, *Phys. Earth Planet. Inter.* **163**, 52 (2007).

[34] S. M. Peacock, Fluid processes in subduction zones, *Science* **248**, 329 (1990).

[35] S. M. Peacock, Numerical simulation of subduction zone pressure-temperature-time paths: constraints on fluid production and arc magmatism, *Philos. Trans. R. Soc. Lond. Ser. A-Math. Phys. Eng. Sci.* **335**, 341 (1991).

[36] B. R. Hacker, G. A. Abers, and S. M. Peacock, Subduction factory: 1. theoretical mineralogy, densities, seismic wave speeds, and H<sub>2</sub>O contents, *J. Geophys. Res.-Solid Earth* **108**, 10.1029/2001JB001127 (2003).

[37] P. E. van Keken, B. R. Hacker, E. M. Syracuse, and G. A. Abers, Subduction factory: 4. depth-dependent flux of H<sub>2</sub>O from subducting slabs worldwide, *J. Geophys. Res.-Solid Earth* **116**, 10.1029/2010JB007922 (2011).

[38] B. R. Hacker, H<sub>2</sub>O subduction beyond arcs, *Geochem. Geophys. Geosyst.* **9**, 10.1029/2007GC001707 (2008).

[39] E. M. Syracuse and G. A. Abers, Global compilation of variations in slab depth beneath arc volcanoes and implications, *Geochem. Geophys. Geosyst.* **7**, 10.1029/2005GC001045 (2006).

[40] T. L. Grove, C. B. Till, M. J. Krawczynski, and R. Jeanloz, The role of H<sub>2</sub>O in subduction zone magmatism, *Annu. Rev. Earth Planet. Sci.* **40**, 413 (2012).

[41] L. H. Rüpke, J. P. Morgan, M. Hort, and J. A. D. Connolly, Serpentine and the subduction zone water cycle, *Earth Planet. Sci. Lett.* **223**, 17 (2004).

[42] C. R. Ranero, J. P. Morgan, K. McIntosh, and C. Reichert, Bending-related faulting and mantle serpentinization at the Middle America trench, *Nature* **425**, 367 (2003).

[43] D. M. Kerrick, Serpentinite seduction, *Science* **298**, 1344 (2002).

[44] S. M. Peacock, Are the lower planes of double seismic zones caused by serpentine dehydration in subducting oceanic mantle?, *Geology* **29**, 299 (2001).

[45] M. Paulatto, M. Laigle, A. Galve, P. Charvis, M. Sapin, G. Bayrakci, M. Evain, and H. Kopp, Dehydration of subducting slow-spread oceanic lithosphere in the Lesser Antilles, *Nat. Commun.* **8**, 10.1038/ncomms15980 (2017).

[46] T. Seno and Y. Yamanaka, Double seismic zones, compressional deep trench-outer rise events, and superplumes, in *Subduction* (American Geophysical Union (AGU), 2013) pp. 347–355.

[47] T. Garth and A. Rietbrock, Order of magnitude increase in subducted H<sub>2</sub>O due to hydrated normal faults within the Wadati-Benioff zone, *Geology* **42**, 207 (2014).

[48] T. Garth and A. Rietbrock, Constraining the hydration of the subducting Nazca plate beneath Northern Chile using subduction zone guided waves, *Earth Planet. Sci. Lett.* **474**, 237 (2017).

[49] I. Grevemeyer, C. R. Ranero, E. R. Flueh, D. Klaeschen, and J. Bialas, Passive and active seismological study of bending-related faulting and mantle serpentinization at the Middle America trench, *Earth Planet. Sci. Lett.* **258**, 528 (2007).

[50] M. D. Behn, P. B. Kelemen, G. Hirth, B. R. Hacker, and H.-J. Massonne, Diapirs as the source of the sediment signature in arc lavas, *Nat. Geosci.* **4**, 641 (2011).

[51] T. L. Grove, N. Chatterjee, S. W. Parman, and E. Medard, The influence of H<sub>2</sub>O on mantle wedge melting, *Earth Planet. Sci. Lett.* **249**, 74 (2006).

[52] C. Sen and T. Dunn, Dehydration melting of a basaltic composition amphibolite at 1.5 and 2.0 GPa: implications for the origin of adakites, *Contrib. Mineral. Petro.* **117**, 394 (1994).

[53] M. S. Drummond, M. J. Defant, and P. K. Kepezhinskas, Petrogenesis of slab-derived trondhjemite-tonalite-dacite/adakite magmas, *Trans. R. Soc. Edinb.-Earth Sci.* **87**, 205 (1996).

[54] M. L. Frezzotti, J. Selverstone, Z. D. Sharp, and R. Compagnoni, Carbonate dissolution during subduction revealed by diamond-bearing rocks from the Alps, *Nat. Geosci.* **4**, 703 (2011).

[55] I. Wada, M. D. Behn, and A. M. Shaw, Effects of heterogeneous hydration in the incoming plate, slab rehydration, and mantle wedge hydration on slab-derived H<sub>2</sub>O flux in subduction zones, *Earth Planet. Sci. Lett.* **353**, 60 (2012).

[56] N. G. Cerpa, I. Wada, and C. R. Wilson, Fluid migration in the mantle wedge: Influence of mineral grain size and mantle compaction, *Journal of Geophysical Research: Solid Earth* **122**, 6247 (2017).

[57] N. G. Cerpa, I. Wada, and C. R. Wilson, Effects of fluid influx, fluid viscosity, and fluid density on fluid migration in the mantle wedge and their implications for hydrous melting, *Geosphere* **15**, 1 (2018).

[58] S. C. Penniston-Dorland, M. J. Kohn, and C. E. Manning, The global range of subduction zone thermal structures from exhumed blueschists and eclogites: Rocks are hotter than models, *Earth Planet. Sci. Lett.* **428**, 243 (2015).